Journal of Wind Engineering & Industrial Aerodynamics 227 (2022) 105055

Contents lists available at ScienceDirect

Journal of Wind Engineering & Industrial Aerodynamics

journal homepage: www.elsevier.com/locate/jweia

On the effects of orthotropic materials in flutter protection of wind turbine flexible blades

A.J. Torregrosa, A. Gil, P. Quintero, A. Cremades *

CMT-Motores Térmicos, Universitat Politècnica de València, Camino de Vera s/n, Valencia, 46022, Spain

ARTICLE INFO

Keywords:
Aeroelasticity
Reduced order model
Wind turbine
Structural coupling
Flutter

ABSTRACT

Decarbonization requirements have extended the use of wind turbines by orders of magnitude. Due to their high stiffness-to-weight ratio, composite materials have been widely used for manufacturing the turbine blades in the recent years. As a consequence of the orthotropic mechanical properties of these materials, the structural behavior of the blade is conditioned by the orientation of the fibers. This article gives a general idea of the benefits of optimizing the composite material ply angle. Along the paper, two different structures are analyzed, a quasi-isotropic material and a structure with oblique fibers. The analysis is conducted using a reduced order model solver which couples a beam element structural solver with the blade element momentum and Theodorsen pitching airfoil theories. The solvers are validated, and then, the flutter conditions are obtained and used to limit the whole operation curve for both blades. The oblique layup structure is evidenced to increase the critical wind velocity by 10% for a defined control law and electrical system. Therefore, the importance of a correct structural analysis is demonstrated to be crucial in the design and manufacturing of the following generation of wind turbine blades.

1. Introduction

The necessity of reducing carbon emissions and increasing renewable power generation has risen the interest in wind energy. Jacobson et al. (2015) stated that the complete conversion from combustion to electrified system in the U.S. by 2050 will require more than 400 k new 5 MW wind turbines. Moreover, the U.S.A. could have satisfied Kyoto Protocol by installing approximately 200 k wind turbines (Jacobson and Masters, 2001). In addition, the percentage of energy generated by wind turbines has been constantly growing with an average increase of 28% since the 1990s (Jacobson et al., 2015). According to Edenhofer et al. (2011), wind energy offers significant power generation potential in the short- and long-term.

As wind turbine farm number has increased, the length of the blades has also been rising, requiring more efficient designs. Indeed, as stated by Yao et al. (2021), in the last 40 years the radius of the wind turbines has increased from 8 m to 111 m. The growth of the blade radius generates higher deflections and increase the aeroelastic effects (Li et al., 2020). As a consequence, as demonstrated by Hansen (2007), wind induced vibrations, which are related to the interaction between the structure and the surrounding flow (Dowell, 2015), might raise with time under strong winds, leading to destructive effects such as divergence (Thomas et al., 2002) or flutter (Sanches et al., 2019). One way of increasing the stiffness of the structure is enlarging the resistant section, which inevitably leads to an increment of the structural mass. Additionally, the use of high stiffness-to-weight materials allows the increase of the natural vibration frequencies of the structure, and thus, the aeroelastic resistance. Therefore, the manufacturing of composite material blades is a hot topic in wind energy research. Moreover, the analysis of composite materials has demonstrated that their orthotropic properties introduce an extra degree of freedom to the system, allowing for optimum aeroelastic designs without weight penalties (Ledermann et al., 2006) and, thus, reducing production costs (Rogers and Kristof, 2003).

Relative to the composite materials, some authors as Paquette et al. (2007) have studied the application of carbon fiber reinforced polymers to the blade structure. In addition, as stated before, these materials may be designed to take profit of the structural couplings presented by Chadra et al. (1990), which improve the aeroelastic behavior of the whole structure. These phenomena can be used as a passive control for the structure deformation (Farsadi et al., 2019) as twist can be increased (wash-in) or decreased (wash-out) as the airfoil plunges in the lift

* Corresponding author.
E-mail address: ancrebo@mot.upv.es (A. Cremades).

https://doi.org/10.1016/j.jweia.2022.105055
Received 14 February 2022; Received in revised form 24 May 2022; Accepted 2 June 2022
Available online 9 June 2022

direction (Stanford et al., 2014).

In order to model wind turbine blade structures, different tools and approaches can be found in the literature. Some authors use Finite Element Analysis (FEA) to calculate the internal strain and stress of the structure (Meng et al., 2015). For instance, Boudounit et al. (2019) used the finite element method to evaluate the potential of composite materials in wind turbine applications and to predict the zones of the structure sensitive to damage. Others have developed lower computational cost procedures, such as dimensional reduction (BERDICHEVSKY et al., 1992). For instance, in Carrera et al. (2013) the vibrational state of a rotor blade, and in Rajpal et al. (2019) the aeroelastic behavior of a wing, were calculated by means of reduced order models.

Relative to the wind turbine aeroelastic problem, Forcier and Joncas (2019) and Li et al. (2020) used the blade element momentum (BEM) theory for simulating the rotor aerodynamics coupled with the geometrically exact beam theory (GEBT) for the structure. Nevertheless, this solver only simulates quasi-steady aerodynamics and it does not include any unsteady aerodynamic model. In addition, the previous work does not evaluate the effects of orthotropic materials on the aeroelastic behavior. Other authors as, Li and Caracoglia (2019) and Pourazarm et al. (2016), have performed reliability analysis of the uncertainties inherent to flutter for isotropic structures using Monte Carlo models. Other works use Computational Solid/Fluid Dynamics (CSD/CFD) (Gil et al., 2021). For instance Kaviani and Nejat (2021) calculated the aeroelastic behavior of the blades and then obtained the resulting acoustic field by using Improved Delayed Detached Eddy Simulations (IDDES), Carrión et al. (Carri ó n et al., 2014) used bar elements to couple with CFD simulated loads and Wang et al. (2016) performed a 1D coupling between the CFD solution and the finite element method used to solve the structure. However, these researches did not simulate the effects of composite material structures.

The current work attempts to extend the research presented before by demonstrating the influence of the layup orientation on the flutter velocity of a wind turbine. The aeroelastic limits of a NREL Phase VI Rotor (Hand et al., 2001) are obtained and applied in combination with the electrical system maximum power to constrain the operation of the wind turbine. The NREL geometry has been chosen as it has been widely analyzed in the literature (Sorensen et al., 2002) and the aerodynamic performance is well known (Torregrosa et al., 2019a). As the objective of the paper is to show the improvement of the structural behavior by orienting the carbon fiber, two generic layups are proposed in this work. Finally, the control law is assumed to maintain the tip speed ratio until a maximum angular velocity is reached. Moreover, the overall generated power is demonstrated to be only dependent of the tip speed ratio inside the stability area.

The article is structured as follows. In Section 2, the methodology of the work is presented: the geometry is described and the models are explained. Then, in Section 3 the main results of the work are shown. The models are validated, the performance of the turbine is analyzed and the effects of the layup are calculated and discussed. Finally, in Section 4 the main conclusions are presented.

2. Methodology

2.1. Case of study

For the analysis, the NREL Phase VI Rotor blades were used. The blade cross-section follows an S809 airfoil which is divided into two cells by a vertical spar located in the mean chord. Two different structures are presented along the article. In both cases, the wall of the section is a laminated layup (plies configuration) of 8 plies. For the first layup (Structure 1), the structure presents 6 internal plies of unidirectional carbon fiber (CFRP) (Qin and Librescu, 2002) with orientation $(90/45/-45)_s$, while the external plies present a quasi-isotropic glass fiber fabric (GFRP) (Mahdi et al., 2006) with the fibers in the orientation 90/0. For the second structure (Structure 2), the skin layup after the transition sections, is modified, using a $(60)_6$ lamination for the internal carbon fiber plies, with the exception of the spar, which maintains the previous layup. Note that the fibers are rotated backwards in both surfaces of the blade. Material properties are presented in Table 1. The previous material properties would correspond to a glass and carbon fiber volume fraction of approximately 27% and 63% respectively according with Vijcic and Dimic (2013) and Singh et al. (2012).

In addition, shell cross-section distortion is prevented by adding dense aluminum ribs at the root, the transitions and the tip and thin walled ribs being located every 2% of the span.

The reference system of the wind turbine blade is presented in Fig. 1. In addition the main displacements of the section are defined: u is the horizontal displacement, v the vertical displacement and θ the twist. Note the inverse direction of the angle of attack α and the twist θ. In the figure, the variables a and a' represent the induced velocities and r is the radial position.

2.2. Aeroelastic model

The aeroelastic behavior of the blade is calculated by combining a structural model with the aerodynamic loads. The mathematical definition of the elastic solid and the acting forces and moments are explained below.

2.2.1. Structural model

The mechanical properties of the structure are obtained from the Librescu and Song (2006) theory, assuming a nonshearable structure with warping. This theory has been previously applied by Qin and Librescu (2002) and Touraj Farsadi (Touraj Farsadi and Sener, 2017) to the thin walled orthotropic beam problem, reducing the 3D problem to a 1D problem. The cross section is calculated for an orthotropic material assuming that the transverse displacements, u, and v, of the section are much larger than the longitudinal displacement w, the surface normal stress can be ignored ($\sigma_{nn} \approx 0$) in the equations, the cross-section remains rigid in its plane, $\varepsilon_{xx} = \varepsilon_{yy} = \varepsilon_{xy} = 0$, and the transverse shear strains remain uniform over the cross section. The cross-section stiffness matrix is calculated from the strain energy definition as in Equation (1).

$$E_V = \frac{1}{2}\int_0^L \vec{D}^T \mathbf{A} \vec{D} dz \tag{1}$$

Here, the matrix **A** has been obtained by integrating stress and strain along the section. A similar procedure is developed for the mass matrix, **M**, by using the kinetic energy, equation (2).

$$E_K = \frac{1}{2}\int_0^L \dot{\vec{D}}^T \mathbf{M}_s \dot{\vec{D}} dz \tag{2}$$

For the definition of the matrices, the reader is referred to AppendixA.

Then, the section solution is integrated along the span of the beam elements in order to obtain global nodal stiffness and mass matrices. Relative to the boundary conditions, clamping conditions are applied over the root to restrain the motion. Moreover, in order to include the ribs into the simulation, an additional boundary condition is imposed at the rib sections to prevent them from warping.

2.2.2. Aerodynamic model

The aerodynamic forces are obtained by calculating their steady and dynamic contributions. The steady contribution is obtained by applying the blade element momentum method (Manwell et al., 2009), which has traditionally been used for the aerodynamic calculations of the rotating blades of wind turbines. In this theory, the normal and tangential induced factor a and a' are obtained by combining the blade element loads with the momentum equation. Then the distribution of forces in the blade are obtained evaluating the aerodynamic coefficients with the effective angle of attack.

Table 1
Material properties of the carbon-fiber and the glass-fiber-reinforced polymer: E_l longitudinal elastic modulus, E_t transverse elastic modulus, G_{lt} longitudinal-transverse shear modulus, G_{tt} transverse-transverse shear modulus, ν_{lt} longitudinal-transverse Poisson's ratio, ν_{tt} transverse-transverse Poisson's ratio, h_{ply} ply thickness, ρ material density.

Material	E_l	E_t	G_{lt}	G_{tt}	ν_{lt}	ν_{tt}	h_{ply}	ρ
Units	(GPa)	(GPa)	(GPa)	(GPa)	(−)	(−)	(mm)	(kg/m^3)
CFRP	141.96	9.78	6.0	4.83	0.42	0.5	0.13	1445
GFRP	20.0	19.0	4.2	4.2	0.13	0.13	0.53	2540

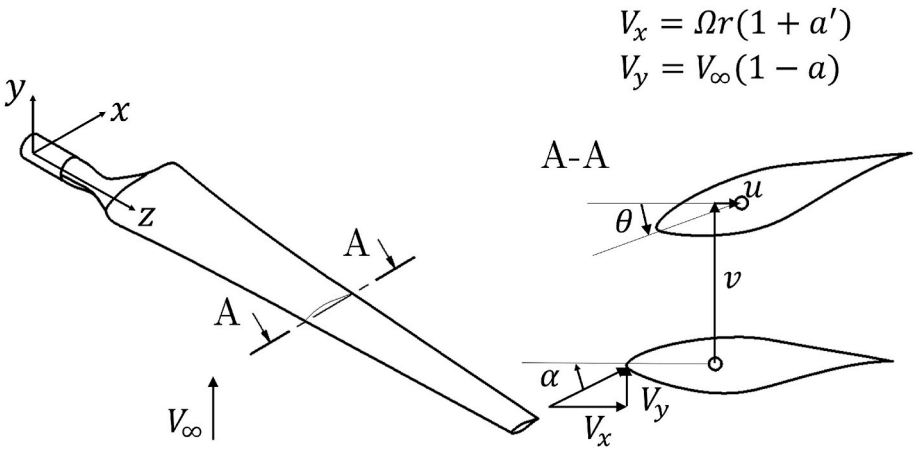

Fig. 1. Reference system of the blade and main displacements of the section.

$$dF_N = \frac{N_b}{2}\rho_\infty\left((V_\infty(1-a))^2 + (\Omega r(1+a'))^2\right)(C_L\cos(\varphi) + C_D\sin(\varphi))cdr == \begin{cases} \rho_\infty V_\infty^2 2b(1-a)\pi r F dr & a < \frac{1}{3} \\ \rho_\infty V_\infty^2 2b\pi r\left(1 - \frac{a}{2}(5-3a)\right)Fdr & a < \frac{1}{3} \end{cases} \tag{3}$$

$$dQ = \frac{N_b}{2}\rho_\infty\left((V_\infty(1-a))^2 + (\Omega r(1+a'))^2\right)(C_L\sin(\varphi) - C_D\cos(\varphi))crdr == 4a'(1-a)\rho V_\infty \pi r^3 \Omega dr \tag{4}$$

Here, N_b is the number of blades, ρ_∞ the free stream density, V_∞ the wind velocity, Ω the rotation speed, c is the airfoil chord, r the radial position of the airfoil, C_L and C_D are lift and drag coefficient respectively and φ is the induced angle, equation (5). Moreover, the tip loss function F is evaluated in equation (6).

$$\tan(\varphi) = \frac{V_\infty}{\Omega R}\frac{1-a}{1+a'} \tag{5}$$

$$F = \left(\frac{2}{\pi}\right)\cos^{-1}\left[\exp\left(-\left\{\frac{N_b(1-r/R)}{2(1-r/R)\sin(\varphi)}\right\}\right)\right] \tag{6}$$

In addition, the three-dimensional behavior of the blade generates extra lift and reduces drag compared to the two-dimensional airfoil. These effects have been corrected using equation (7) from Chaviaropoulos and Hansen (2000).

$$C_{X,3D} = C_{X,2D} + 2.2(c/r)\cos^4(\theta)\Delta C_X \tag{7}$$

where $X = L, D, M$ references the lift, drag and moment coefficients. The parameter ΔC_x is calculated in Equation (8).

$$\Delta C_L = C_{L,\text{inv}} - C_{L,2D};\ \Delta C_D = C_{D,2D} - C_{D,2D-\min};\ \Delta C_M = C_{M,\text{inv}} - C_{M,2D} \tag{8}$$

The transient effects are obtained from Theodorsen (1935) theory, applying a Fourier inverse transform for the obtainment of the aerodynamic coefficients in the time domain (Dowell, 2015) and the Duhamel transformation in order to evaluate the dynamic load as a

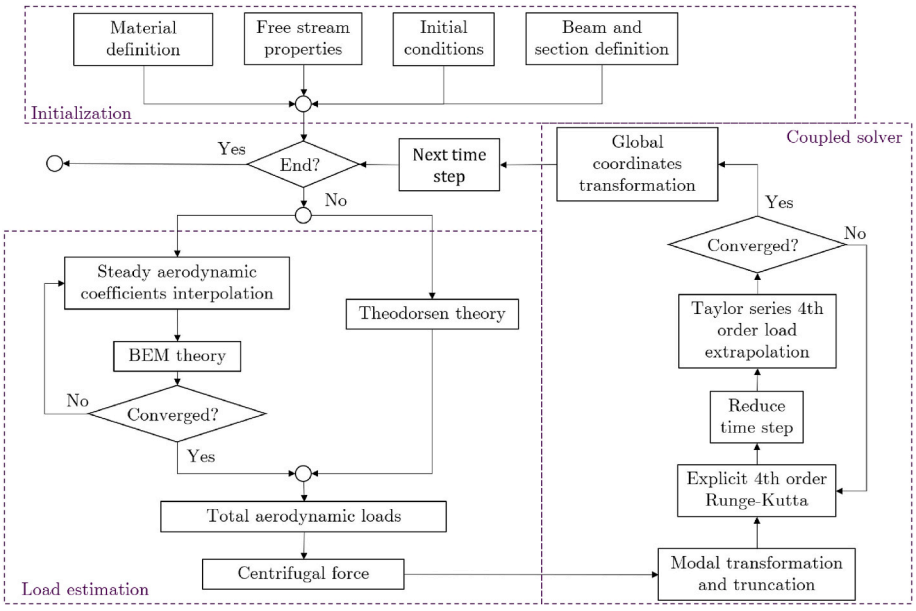

Fig. 2. Schematic flowchart of the coupled system solver.

superposition of impulses, equation (9), where the complex function $C(k)$ is simplified using Wagner's function, equation (10).

$$L(t) = \pi\rho b^2\left(-\frac{d^2v}{dt^2} - V_\infty\frac{d\theta}{dt} + bx_a\frac{d^2\theta}{dt^2}\right) - 2\pi\rho V_\infty b\left(w_a(0)\kappa(s) + \int_0^s \frac{dw_a}{d\sigma}(\sigma)\kappa(s-\sigma)d\sigma\right) \quad (9)$$

$$\kappa(s) = 1 - 0.165e^{-0.0455\ s} - 0.355e^{0.3\ s} \quad (10)$$

Being the function w_a and the variable s defined by equation (11).

$$w_a = \frac{dv}{dt} + V_\infty\theta + b\left(\frac{1}{2} - x_a\right)\frac{d\theta}{dt}\ ;\ s = \frac{tV_\infty}{b} \quad (11)$$

2.2.3. Coupled system

The aerodynamic and the structural models are simultaneously solved using a coupled solver, consisting of three main blocks: initialization, load modeling and displacement calculation. Fig. 2 shows a schematic flowchart for the calculation process.

In the first block, the structure of the blade is defined: the material and geometry are selected. Then the cross-section mechanical properties are calculated and integrated along the beam. In addition, the free stream properties and initial conditions are specified.

The aerodynamic loads are calculated in the load modeling block. The previously explained blade element momentum theory is applied at each cross-section of the beam, interpolating the aerodynamic coefficient from a CFD polar. After convergence is reached, the transient forces described in Theodorsen (1935) are added to the solution. Then, the centrifugal force is added to the total aerodynamic load.

Finally, the displacements of the structure are updated by integrating the dynamic equation of the system. The problem is solved in the modal form, using a modal truncation of the first six modes. The system is normalized in equation (12).

$$\mathbf{M}\ddot{\vec{u}} + \mathbf{K}\vec{u} = \vec{F} \rightarrow \mathbf{M}^{-1/2}\mathbf{M}\mathbf{M}^{-1/2}\ddot{\vec{q}} + \mathbf{M}^{-1/2}\mathbf{K}\mathbf{M}^{-1/2}\vec{q} = \mathbf{M}^{-1/2}\vec{F} \quad (12)$$

where $\vec{u} = \mathbf{M}^{-1/2}\vec{q}$. Then, the mode shapes are truncated so the final deformation of the beam, $\vec{u}$, can be expressed in terms of the n first modal weights $\vec{y}$, Equation (13), multiplying by the modal matrix $\mathbf{\Psi}$.

$$\mathbf{\Psi}^T\mathbf{M}^{-1/2}\mathbf{M}\mathbf{M}^{-1/2}\mathbf{\Psi}\ddot{\vec{y}} + \mathbf{\Psi}^T\mathbf{M}^{-1/2}\mathbf{K}\mathbf{M}^{-1/2}\mathbf{\Psi}\vec{y} = \mathbf{\Psi}^T\mathbf{M}^{-1/2}\vec{F} \quad (13)$$

The solution is calculated with an adaptive time step fourth-order

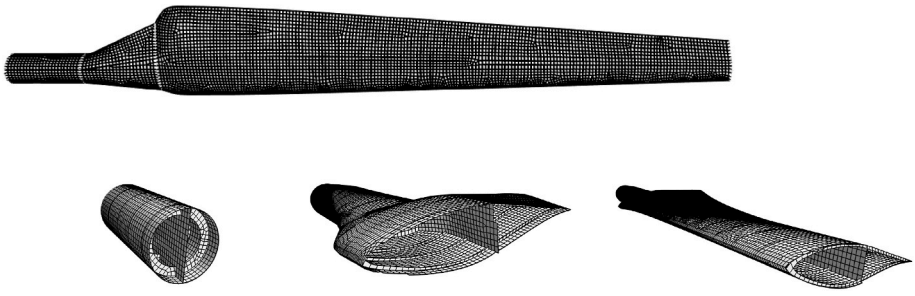

Fig. 3. Mesh of the blade. Detail of the cross section for the cylindrical, transition and S809 zones. Skin, spar and dense and thin-walled ribs are included.

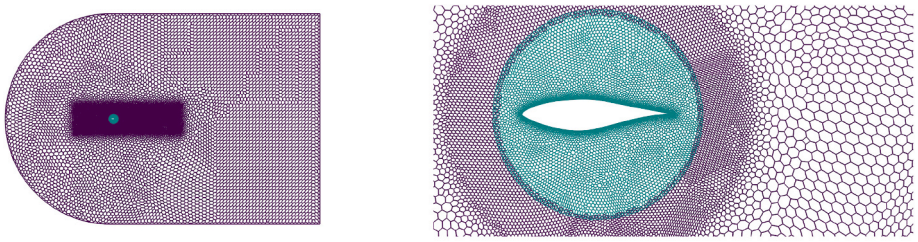

(a) CFD mesh. (b) Detail on the overset region.

Fig. 4. CFD mesh and detail of the overset region.

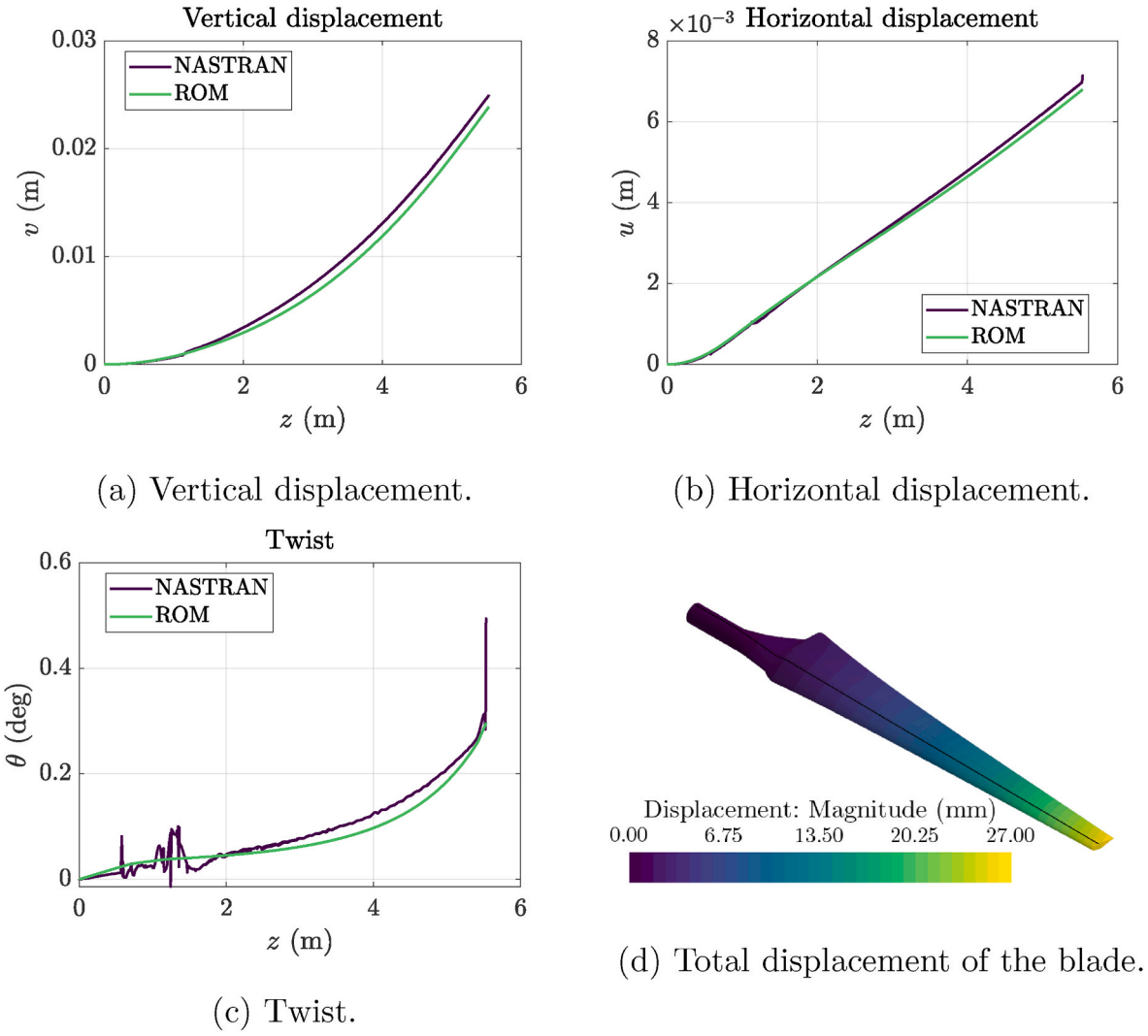

(a) Vertical displacement. (b) Horizontal displacement.

(c) Twist. (d) Total displacement of the blade.

Fig. 5. Deformation of the blade under static loads: $F_y = 100$ N, $F_x = 100$ N, $M_z = 100$ N m. The longitudinal black line of Fig. 5d presents the geometrical center of rotation where the displacements are measured. In the Figure, v is the vertical displacement, u the horizontal displacement and θ the twist.

Runge-Kutta method, AppendixB. The time step is reduced internally at each iteration, extrapolating with Taylor series the applied forces. When convergence is achieved, the solution is transformed into nodal displacements and the time step is advanced.

2.3. Computational solid dynamics

The structure definition presented in Section 2.2.1 was validated against a computational solid simulation. This simulation was calculated with NASTRAN using a composite laminate shell mesh. The solid was meshed using a final grid of $1.2 \cdot 10^4$ quadrilateral parabolic elements, which ensure a low discretization error, see Fig. 3. This figure shows the finite element mesh of the external shell, the internal ribs and the spar. This mesh is used for calculating linear elasticity analysis for obtaining both steady deformation and vibration modes (see Fig. 4).

2.4. Computational fluid dynamics

The Theodorsen transient loads are tested with a pitching and plunging airfoil CFD simulation. This simulation has been performed

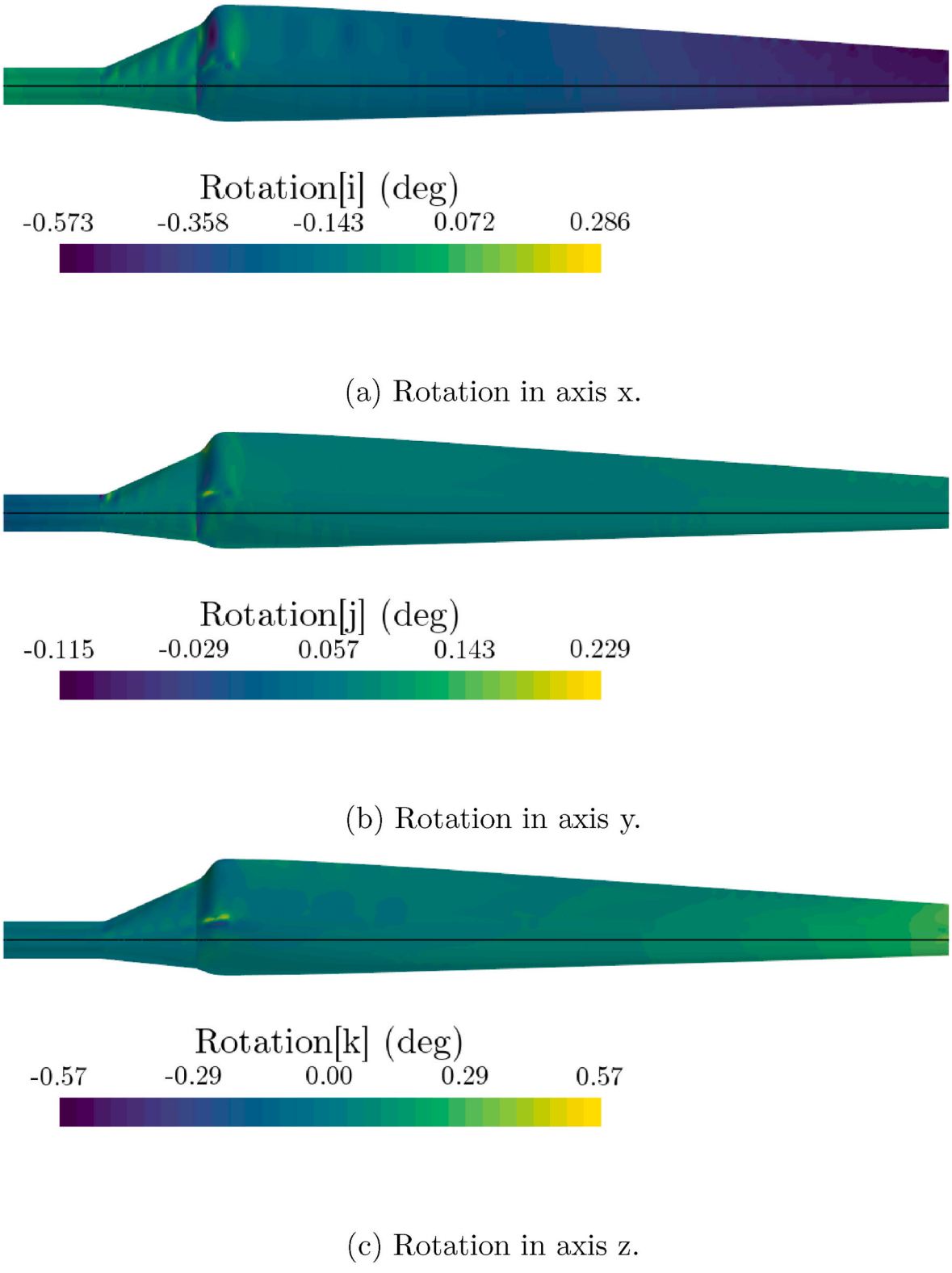

Fig. 6. Rotation of the shell elements. The geometrical rotation axis is marked over the surface.

using the proprietary software Simcenter Star-CCM+. The discretization of the domain is made using an overset mesh strategy and a polygonal mesh. The conservative equations of the fluid are computed with a coupled solver with second order upwind ROE FDS scheme for the advection terms (Weiss et al., 1999), (Weiss and Smith, 1995). The gradients are calculated using the Gauss-Least Squares Method with the Venkatakrishnan limiter (Venkatakrishnan, 1995).

3. Results

In this section, the main results obtained are shown and discussed. The mathematical model was validated for the structural and the aerodynamic submodels. On the one hand, the structure was compared with NASTRAN finite element simulations. Firstly, the deformation of the blade under a static load in the tip was simulated. Then, the vibration

Table 2
Natural frequencies of the first four vibration modes.

Solver	Mode 1 (Hz)	Mode 2 (Hz)	Mode 3 (Hz)	Mode 4 (Hz)
NASTRAN	4.647	6.504	21.494	48.951
ROM	4.456	6.430	19.794	48.067
Deviation (%)	4.11	1.15	8.82	1.81

modes were obtained. On the other hand, a comparison between the aerodynamic blade element model and the results of previous works (Torregrosa et al., 2019b) was performed to validate the aerodynamic model. Finally, the models were coupled and the dynamic behavior of the turbine was analyzed. The aeroelastic limits were obtained and the operation capabilities of both structures were compared.

3.1. Structure validation

In order to demonstrate its accuracy, the Reduced Order Model has been validated against a NASTRAN Finite Element Analysis. Firstly, the stiffness of the blade was checked by means of a steady analysis. Then the vibration modes and the modal shape were studied obtaining the frequency error.

For testing the blade stiffness, a steady study was defined. A combination of forces and moments was applied to the tip section in the geometrical rotation axis: vertical (F_y) and horizontal (F_x) forces of 100 N and a twisting moment (M_z) of 100 N m. Fig. 5 shows the deformation of the blade in the static test, evidencing that the ROM presents a high accuracy for the vertical and horizontal deformation of the tip section with respect to the FEA model. Nevertheless, the FEA twist presents higher errors such as the sawtooth behavior near the root.

In addition, in order to analyze the distortion of the cross-section of the blade, the rotation of the shell elements in the three axis is shown in Fig. 6. In the Figure, the effect of the ribs is observed as the rotation of the elements is restrained over them. The shell effects are conditioning the rotation of the section, and thus, they are the main source of the differences with respect to the 1D simulation. Thus, the ribs are required for maintaining the shape of the cross-section and are necessary to match the 1D behavior.

Moreover, the vibration modes were analyzed. Table 2 compares the first 4 vibration modes of the blade which are expected to influence the dynamic behavior of the structure. Both models agree with a maximum error of 9%. Therefore, the structural ROM is able to reproduce both stiffness and mass properties and can be used in the elastic analysis of the blade, allowing to reduce computational cost with respect to a 3D finite element analysis. Additionally, Fig. 7 shows the modal shape of the blade. Similar deformation shapes are obtained for the ROM and NASTRAN models, as can be tested in the Modal Assurance Criterion (MAC) of Fig. 8 (Torregrosa et al., 2019a). In this figure, the darkest the color, the higher the correlation. The diagonal of the matrix is demonstrated to present values close to the unity, thus, both models correlate. It is apparent that the problem is dominated by bending modes, as a result of the high torsional stiffness of the multicell cross-section of the blade,

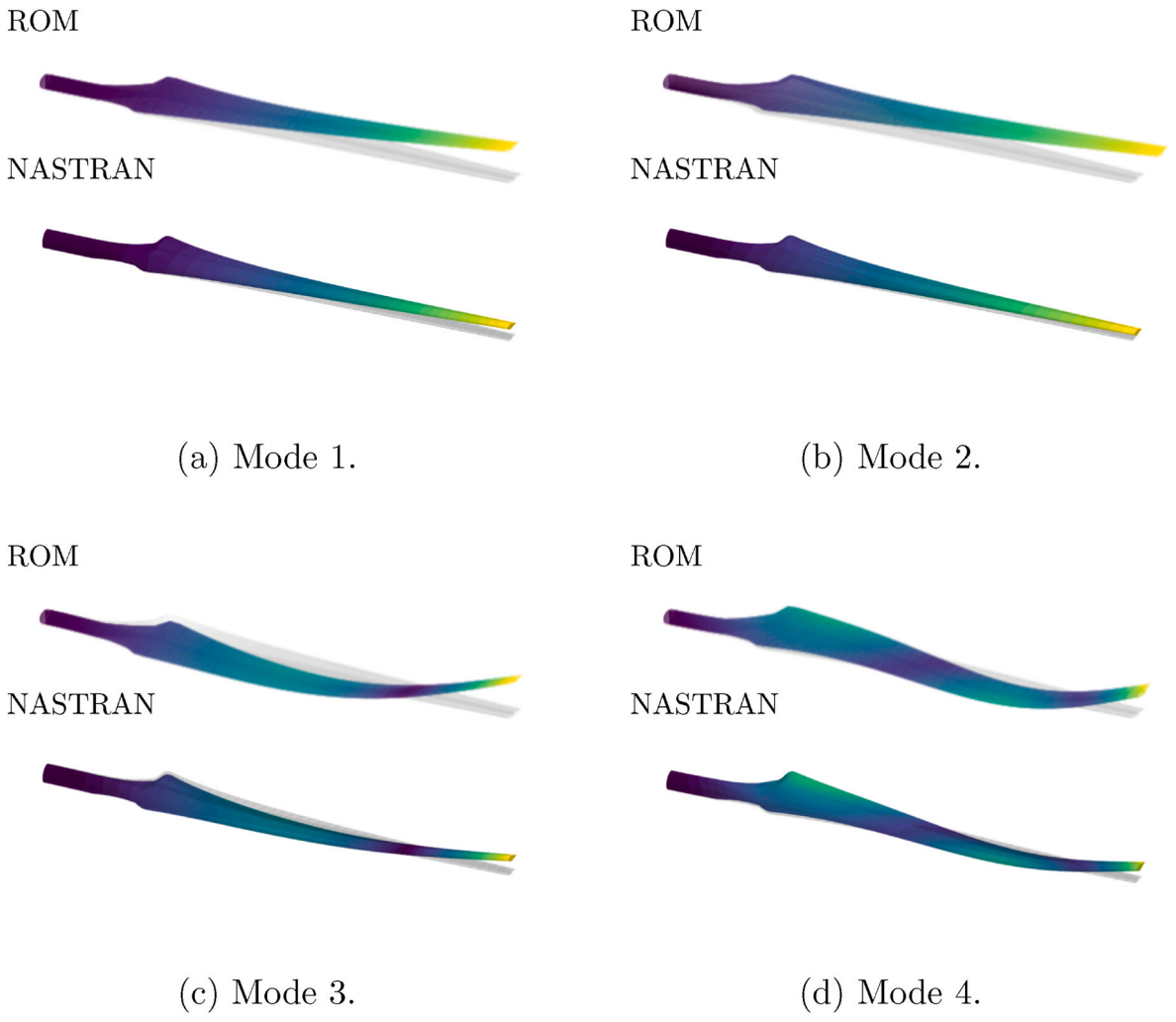

Fig. 7. Vibration modes obtained from the 1D reduced order model.

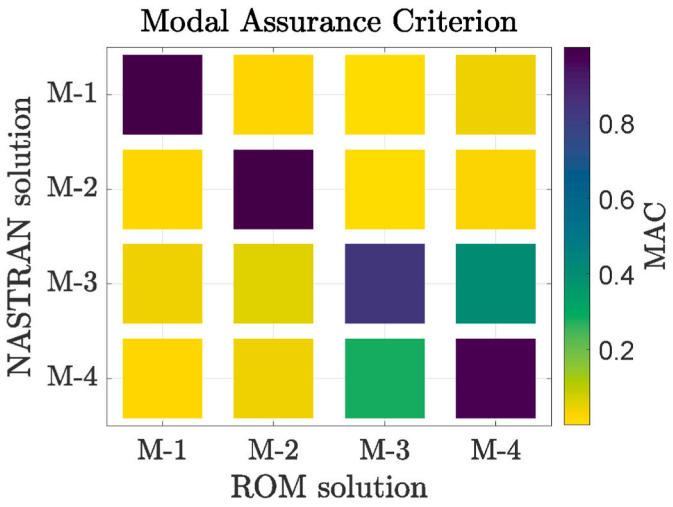

Fig. 8. Modal assurance criterion.

although modes 3 and 4 include bending-torsion couplings.

3.2. Validation of the wind turbine aerodynamic characteristics

The aerodynamic blade element momentum model acting over the wind turbine surface was validated against the experimental data of Lee et al. (2017) for a tip speed ratio of $\lambda = 6$, Fig. 9a, where the predicted force coefficient is lightly higher for the BEM model. Indeed, the power coefficient curves are compared in Fig. 9b with the CFD and experimental data of Torregrosa et al. (2019b), showing a difference in the maximum power peak. According with Plaza et al. (2015), the maximum power peak in the BEM appears for lower values of the tip speed ratio. This fact is consistent with the force distribution results as the BEM model overpredicts the loads. However, the methodology reduces by orders of magnitude the computational cost, and therefore, it speeds up the initial stages of the aerodynamic design with an acceptable prediction of the loads.

In addition, the transient loads calculated with Theodorsen's theory are compared to a pitching and plunging airfoil, Equation (14).

$$\theta(t) = \overline{\theta} + 2.5sin(20\pi t); \quad v(t) = 0.01sin(8\pi t) \tag{14}$$

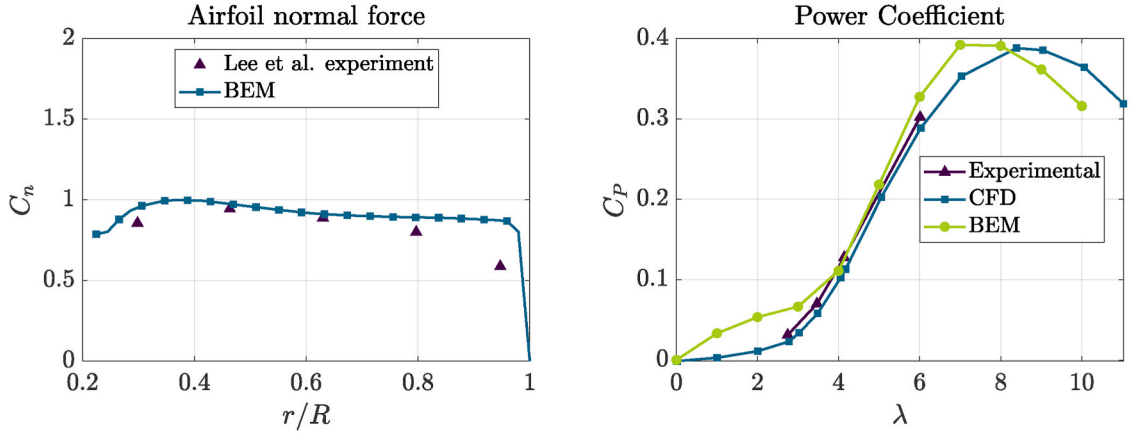

(a) Normal force coefficient distribution for a wind velocity of 7 m/s and a rotation velocity of 73 rpm.

(b) Blade Element Momentum validation with CFD and experimental data.

Fig. 9. Aerodynamic validation of the BEM.

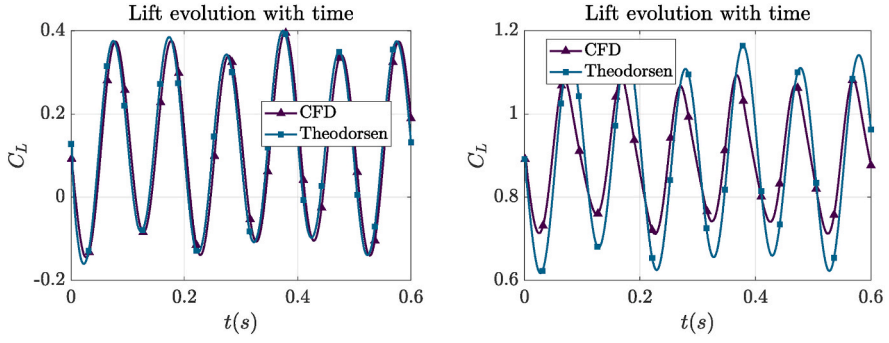

(a) Validation for mean incidence of 0 deg.

(b) Validation for mean incidence of 8 deg.

Fig. 10. Aerodynamic validation of Theodorsen model.

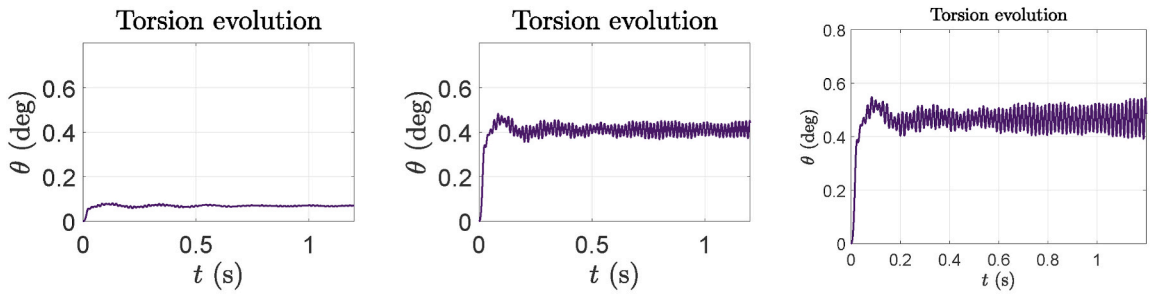

(a) Structure 1: $\lambda = 7$, $E^* = 500$ (b) Structure 1: $\lambda = 7$, $E^* = 80$ (c) Structure 1: $\lambda = 7$, $E^* = 62$

Fig. 11. Torsion evolution for structure 1 under different operation points.

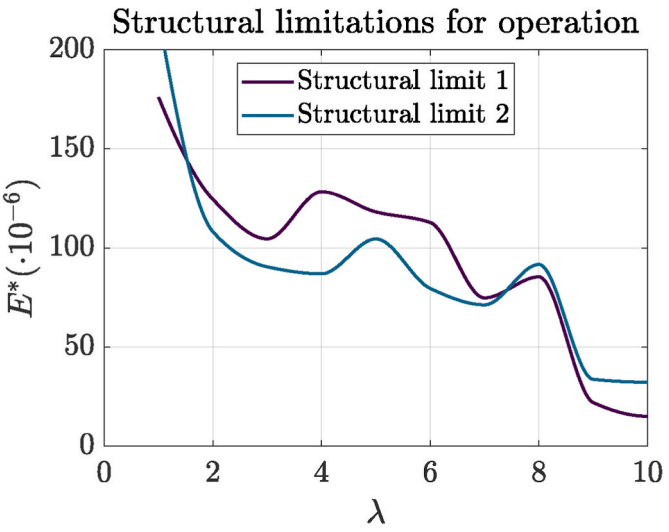

Fig. 12. Limitations of the structure for nondimensional variables.

The lift coefficient obtained by the ROM and the CFD is presented in Fig. 10b. In the figure, two validation cases are presented. The first simulation is performed for a mean incidence $\overline{\theta} = 0$ deg, while the second is calculated for $\overline{\theta} = 8$ deg. Note that the transient Theodorsen's model supposes an attached flow, for this reason, the accuracy of the solution is higher for low incidence angles. Nevertheless, in the point of maximum efficiency of the blade, approximately 8 deg of incidence, the model reduces its accuracy. However, due to its efficient computational cost and the low deviation from CFD simulations, it is applied on this work.

3.3. Elastic wind turbine solution: prediction of flutter speed

The previous structural and aerodynamic models were coupled in order to calculate the aeroelastic behavior of the blade. The structural displacement was obtained for different operation points (wind and rotation velocities), in terms of the characteristic parameters of the simulations: tip speed ratio $\left(\lambda = \frac{\Omega R}{V_\infty}\right)$ and non dimensional elastic modulus $\left(E^* = \frac{E_l}{\frac{1}{2}\rho_\infty V_\infty^2 (1+\lambda^2)}\right)$. The mean twist is analyzed for the structurally stable operations. The stability is limited by defining two consecutive intervals in the time evolution, Fig. 11 and measuring the evolution of the amplitude. The range of intervals have been selected in order to contain twice the first natural frequency of the structure. In this figure, three different conditions are presented: damped (Fig. 11a), limit cycle (Fig. 11b) and unstable (Fig. 11c).

The instability condition is determined from the computed time signals, when negative damping is detected in the time evolution of the torsion (the amplitude of the oscillations tend to increase its value with time). Fig. 12 shows the aeroelastic limits of both structures. In the figure, structure 2 is demonstrated to improve the aeroelastic limitations in the range between $\lambda = 2$ and $\lambda = 7$, when the bending-twisting coupling effect compensates the unsteady aerodynamic loads.

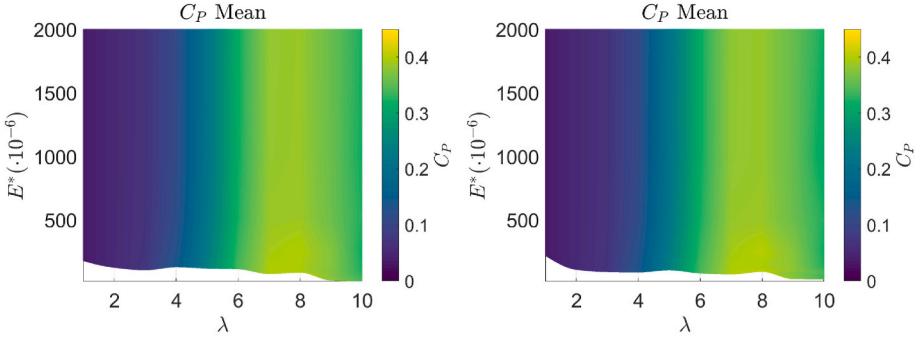

(a) Structure 1. (b) Structure 2.

Fig. 13. Mean value of the power coefficient of the structures for the different operation conditions.

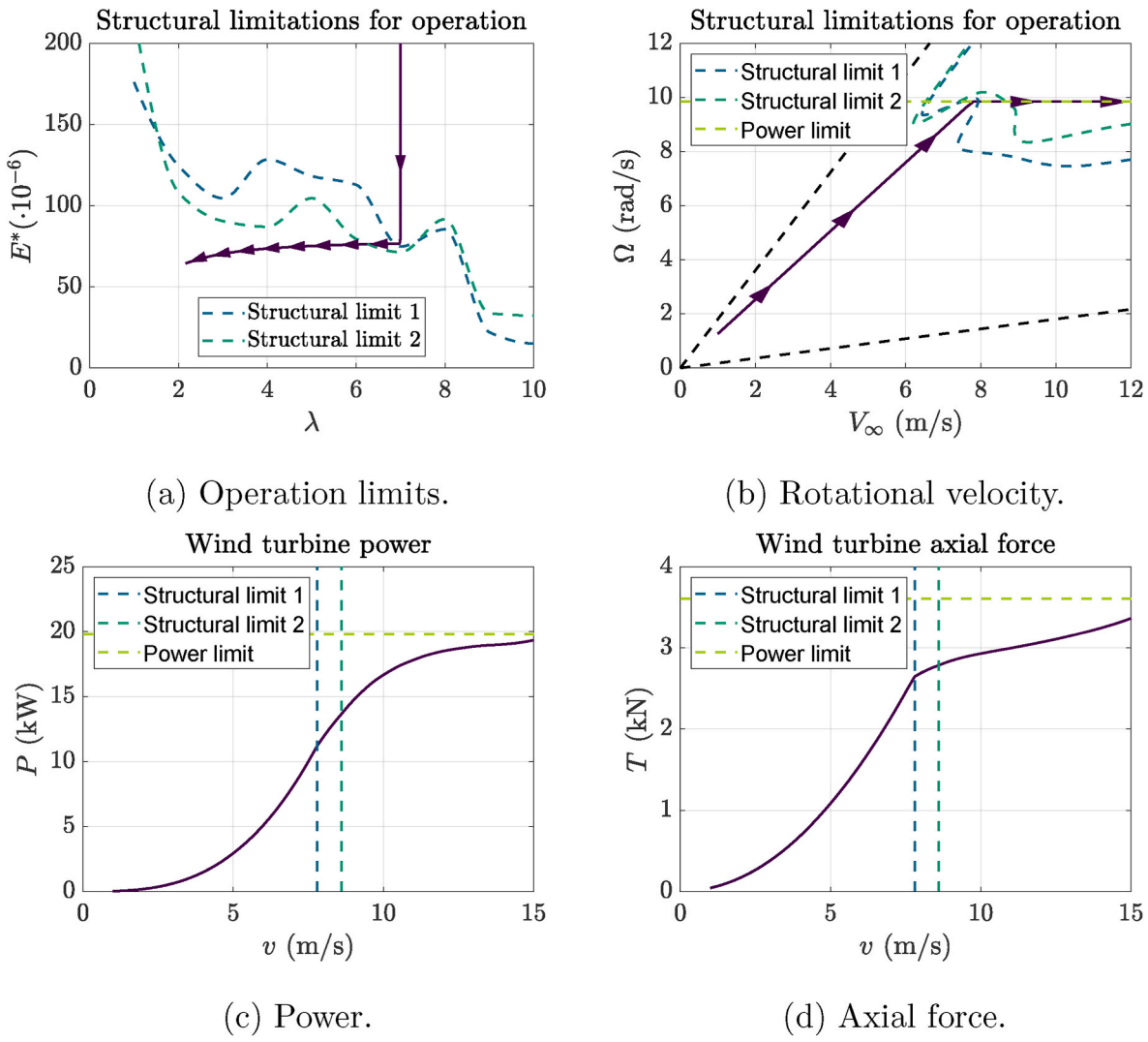

Fig. 14. Operation curves of the wind turbine. The dashed lines represent the structural and electrical limitations of the system whereas the solid curves represent operation of the turbine.

3.4. *Wind turbine range of operation*

In this subsection, the deformation information of Fig. 12 is used for limiting the operation of the turbine. Inside the stability limits, the mean values of the power coefficient are evaluated due to the interest of demonstrating that the reduction of nondimensional stability produces negligible effects on the power generation for these structures, as it mainly depends on the tip speed ratio. The power coefficient for both structures is presented in Fig. 13. Therefore, in the operation analysis of both turbines the generation of power can be evaluated using the rigid rotor performance coefficients. Then, the maximum allowed wind velocity is limited using the elastic blade information for the characteristic dimensionless parameters.

Relative to the control law, the turbine can rotate at optimum tip speed ratio ($\lambda \approx 7$) until the maximum rotation velocity is reached. This maximum angular velocity is limited in order to generate the maximum power for the values of the wind velocity in which the power derivative remains low or null. Higher values of the power could damage the electrical system. Accordingly with the literature (Hand et al., 2001), the rated power of the turbine is 19.8 kW. Once the rated power is reached, a constant rotational velocity is imposed to the system. The power and rotational velocity curves are presented in Fig. 14 together with the structural and electrical limitations.

The curves of Fig. 14 show the increase in the range of wind in which the turbine could operate. Fig. 14a shows the control law of the turbine in terms of the nondimensional variables. The solid dark line represents the value of the different dimensionless parameters as the wind velocity is increased (direction of the arrow heads) following the control law of Fig. 14b. The dashed lines state the physical limitations of the system for both structures and the electrical generator. The intersection between the solid line and the dashed lines supposes the collapse of the structure, as the deformation will be amplified with time. In the figure, it is evidenced that rotating backwards the fibers delays the instability. In dimensional terms, the power generated by the rotor is presented as a function of the wind velocity in Fig. 14c. The figure shows the increase wind velocity of the structural limit produced by the reorientation of the fibers. The oblique fiber structure is demonstrated to produce an improvement of approximately 10% in the maximum wind velocity of the system. When the material is rotated, the structural limitation is overcome and the wash-in delays the flutter effects for the same structural weight (29.6 kg) of the blade. In addition, the modified structure may load higher axial forces, Fig. 14d; therefore, the tower and blades should also be calculated under static loads to prevent static failure.

4. Conclusions

The aeroelastic behavior of a carbon-fiber-reinforced polymer wind turbine blade was analyzed in order to provide a general idea of the

effects of fiber orientation influence. The structural integrity of the blade has been evaluated for two different layups. The first configuration, Structure 1, presents a quasi-isotropic layup. A modification on the fiber orientation was proposed for the second layup, Structure 2. In this case, the unidirectional fibers were rotated backward, creating negative bending-torsion structural coupling, which is related with load alleviation (Stanford et al., 2014). The results obtained open the possibility of future work to evaluate the optimum layup configuration and to validate the elastic results with high computational cost simulations or experimental data. Main findings of the work are summarized below:

- Beam element structural model has been proven to predict the blade steady deformation with an error lower than 5% and the natural modes with less than 9%.
- Blade element momentum methodology and Theodorsen's theory are demonstrated to provide accurate results with a low computational cost comparing with experimental data and CFD simulations.
- The power coefficient has been demonstrated to depend exclusively of the tip speed ratio in the stable region.
- Flutter velocity has been calculated for both structures showing higher limits, in the operation conditions, for the oriented fibers (structure 2). Indeed, structure 2 has demonstrated to increase the maximum allowable wind velocity in 10%.

Data availability

The raw/processed data required to reproduce these findings cannot be shared at this time due to technical or time limitations.

CRediT authorship contribution statement

A.J. Torregrosa: Project administration, Writing – review & editing. **A. Gil:** Resources, Writing – review & editing. **P. Quintero:** Conceptualization, Supervision, Writing – review & editing. **A. Cremades:** Conceptualization, Methodology, Software, Validation, Investigation, Writing – original draft, Visualization.

Declaration of competing interest

The authors declare that they have no known competing financial interests or personal relationships that could have appeared to influence the work reported in this paper.

Acknowledgement

This project have been partially funded by Spanish Ministry of University through the University Faculty Training (FPU) program with reference FPU19/02201.

Symbols

α	Angle of attack
ΔC_D	Increment of drag coefficient
ΔC_L	Increment of lift coefficient
ΔC_M	Increment of moment coefficient
Δt_i	Increment of time step
ε_{ij}	Strain in the direction ij
θ	Twist
$\overline{\theta}$	Mean incidence
κ	Wagner function
λ	Tip speed ratio
ν_{lt}	Longitudinal-transverse Poisson's ratio of the laminate ply
ν_{tt}	Transverse-transverse Poisson's ratio of the laminate ply to the elastic axis
φ	Rotation in the axis x
φ	Induced angle
ψ	Rotation in the axis y
$\mathbf{\Psi}$	Modal matrix
ρ	Density of the material
ρ_∞	Density of the air
σ_{ij}	Stress in the direction ij
Ω	Rotation velocity of the wind turbine
a	Induced factor in the normal direction
a'	Induced factor in the tangential direction
$\mathbf{A}$	Cross-section stiffness matrix
b	Semichord of the airfoil
$\overrightarrow{b}$	Vector of the system
c	Chord of the beam
C	Theodorsen complex function
C_D	Drag coefficient
$C_{D,2D}$	2D drag coefficient
$C_{D,3D}$	3D effect drag coefficient
$C_{D,2D-\min}$	Minimum drag
C_L	Lift coefficient
$C_{L,2D}$	2D lift coefficient
$C_{L,3D}$	3D effect lift coefficient
$C_{L,\text{inv}}$	Inviscid lift coefficient
C_M	Moment coefficient
$C_{M,2D}$	2D moment coefficient

$C_{M,3D}$	3D effect moment coefficient
$C_{M,\text{inv}}$	Inviscid moment coefficient
C_n	Normal force coefficient
C_P	Power coefficient
$\overrightarrow{D}$	Degrees of freedom vector
E^*	Dimensionless stiffness
E_K	Kinetic energy
E_l	Longitudinal elastic modulus of the laminate ply
E_t	Transverse elastic modulus of the laminate ply
E_V	Deformation energy
F	Tip loss function
$\overrightarrow{F}$	Force vector
F_N	Axial force of the wind turbine
F_x	Force in x axis
F_y	Force in y axis
G_{lt}	Longitudinal-transverse shear modulus of the laminate ply
G_{tt}	Transverse-transverse shear modulus of the laminate ply
h_{ply}	Thickness of the laminate ply
k	Reduced frequency
$\mathbf{K}$	Stiffness matrix
L	Lift force
$\mathbf{M}$	Mass matrix
$\mathbf{M_A}$	System matrix
$\mathbf{M_s}$	Cross-section mass matrix
M_z	Moment in z axis
N_b	Number of blades
P	Power of the turbine
$\overrightarrow{q}$	Normalized system displacement vector
Q	Torque of the blade
$\overline{\mathbf{Q}}$	Constitutive matrix in the beam element frame
R	Radius of the blade
r	Radial position
s	Nondimensional time
t	Time
T	Rotor axial force
u	Horizontal displacement
$\overrightarrow{u}$	Displacement vector
V_∞	Wind velocity
v	Vertical displacement
V_x	Velocity in the x direction
V_y	Velocity in the y direction
w	Longitudinal displacement
x, y, z	Coordinates of the reference frame
x_a	Position of the elastic axis
$\overrightarrow{x}_t$	Solution vector
$\overrightarrow{y}$	Modal weights

Appendix A. Structural model: cross-section matrices

In this appendix the cross-section stiffness and mass matrices for the non-shearable beam model are presented. Relative to the stiffness matrix **A**, equation (A1) shows its definition. Here the linear displacements in coordinates x, y, z are denoted by u, v, w, and the variables φ, ψ and θ their respective angles.

$$\mathbf{A} = \begin{bmatrix} a_{11} & a_{12} & a_{13} & a_{16} & a_{17} \\ & a_{22} & a_{23} & a_{26} & a_{27} \\ & & a_{33} & a_{36} & a_{37} \\ & & & a_{66} & a_{67} \\ & & & & a_{77} \end{bmatrix} \text{ being } \overrightarrow{D} = \begin{Bmatrix} w_0' - u_0'' - v_0'' \\ \theta' - \theta'' \end{Bmatrix} \tag{A1}$$

The elements of the of the matrix are presented in equations (A2) to A10.

$$a_{11} = \int K_{11} ds;\ a_{12} = \int [K_{11} x + K_{14}(dy/ds)]ds \tag{A2}$$

$$a_{13} = \int [K_{11} y + K_{14}(dx/ds)]ds;\ a_{16} = \int [K_{11}\overline{F} + K_{14} r_t]ds \tag{A3}$$

$$a_{17} = \int K_{13} ds;\ a_{22} = \int \left[K_{11} x^2 + 2x K_{14} \frac{dy}{ds} + K_{44} \left(\frac{dy}{ds} \right)^2 \right] ds \tag{A4}$$

$$a_{23} = \int \left[K_{11} xy - x K_{14} \left(\frac{ds}{ds} \right) + y K_{14} \left(\frac{dy}{ds} \right) - K_{44} \left(\frac{dx}{ds} \right) \left(\frac{dy}{ds} \right) \right] ds \tag{A5}$$

$$a_{26} = \int \left[K_{11} x \overline{F} - K_{14} x r_t + \overline{F} K_{14} \left(\frac{dy}{ds} \right) - K_{44} r_t \left(\frac{dy}{ds} \right) \right] ds \tag{A6}$$

$$a_{27} = \int \left[K_{13} x + K_{43} \left(\frac{dy}{ds} \right) \right] ds;\ a_{33} = \int \left[K_{11} y^2 + 2y K_{14} \frac{dx}{ds} + K_{44} \left(\frac{dx}{ds} \right)^2 \right] ds \tag{A7}$$

$$a_{36} = \int \left[K_{11} y \overline{F} - K_{14} y r_t + \overline{F} K_{14} \left(\frac{dx}{ds} \right) - K_{44} r_t \left(\frac{dx}{ds} \right) \right] ds \tag{A8}$$

$$a_{37} = \int \left[K_{13} y + K_{43} \left(\frac{dx}{ds} \right) \right] ds;\ a_{66} = \int \left[K_{11} \overline{F}^2 - 2 K_{14} \overline{F} r_t + K_{44} r_t^2 \right] ds \tag{A9}$$

$$a_{67} = \int [K_{13} \overline{F} - K_{43} r_t] ds;\ a_{77} = \delta_c \int \Psi K_{23} ds + 2 \int K_{53} ds \tag{A10}$$

The stiffness parameters K_{ij} are obtained from equation (A11).

$$\begin{aligned}
K_{11} &= A_{22} - \frac{A_{12}^2}{A_{11}} \\
K_{13} &= \Psi \left(A_{26} - \frac{A_{12} A_{16}}{A_{11}} \right) + 2 \left(B_{26} - \frac{A_{12} B_{16}}{A_{11}} \right) \\
K_{14} &= B_{22} - \frac{A_{12} B_{12}}{A_{11}} \\
K_{23} &= \Psi \left(A_{66} - \frac{A_{16}^2}{A_{11}} \right) + 2 \left(B_{66} - \frac{A_{16} B_{16}}{A_{11}} \right) \\
K_{43} &= \Psi \left(B_{26} - \frac{B_{12} A_{16}}{A_{11}} \right) + 2 \left(D_{26} - \frac{B_{12} B_{16}}{A_{11}} \right) \\
K_{44} &= 2 \left(D_{22} - \frac{B_{12}^2}{A_{11}} \right) \\
K_{53} &= \Psi \left(B_{66} - \frac{B_{16} A_{16}}{A_{11}} \right) + 2 \left(D_{66} - \frac{B_{16}^2}{A_{11}} \right)
\end{aligned} \tag{A11}$$

being the terms A_{ij}, B_{ij} and D_{ij} defined in equation (A12), where the parameter $\overline{Q}_{ij}^{(k)}$ is the element of the constitutive matrix of the (k) ply.

$$(A_{ij}, B_{ij}, D_{ij}) = \sum_{k=1}^{M} \int_{h_{k-1}}^{h_k} \overline{Q}_{ij}^{(k)} (1, n, n^2) dn \tag{A12}$$

Respect to the mass matrix, equation (A13) shows its definition.

$$\mathbf{M} = \begin{bmatrix}
m_{11} & 0 & 0 & 0 & 0 & m_{16} & 0 \\
 & m_{22} & 0 & 0 & 0 & m_{26} & 0 \\
 & & m_{33} & m_{34} & m_{35} & 0 & m_{37} \\
 & & & m_{44} & m_{45} & 0 & m_{47} \\
 & & & & m_{55} & 0 & m_{57} \\
 & & & & & m_{66} & 0 \\
 & & & & & & m_{77}
\end{bmatrix} \text{ being } \vec{D} = \begin{Bmatrix} w_0 \\ u_0 \\ v_0 \\ \varphi \\ \psi \\ \theta - \theta' \end{Bmatrix} \tag{A13}$$

where the elements are calculated in equations (A14) to A19.

$$m_{11} = m_{22} = m_{33} = b_1;\ m_{16} = -m_{34} = -b_2 + \delta_n \widehat{b}_2 \tag{A14}$$

$$m_{26} = m_{35} = b_3 + \delta_n \widehat{b}_3;\ m_{44} = b_4 + \delta_n b_{14} - 2\delta_n \widehat{b}_8 \tag{A15}$$

$$m_{55} = b_5 + \delta_n \widehat{b}_{15} + 2\delta_n \widehat{b}_9;\ m_{66} = b_4 + b_5 + \delta_n (b_{14} + b_{15}) + 2\delta_n (\widehat{b}_9 - \widehat{b}_8) \tag{A16}$$

$$m_{77} = b_{10} + \delta_n b_{18} - 2\delta_n \widehat{b}_7;\ m_{37} = -b_7 + \delta_n \widehat{b}_1 \tag{A17}$$

$$m_{47} = -b_8 - \delta_n b_{16} + \delta_n \widehat{b}_5;\ m_{57} = -b_9 + \delta_n b_{16} + \delta_n \widehat{b}_5 \tag{A18}$$

$$m_{45} = b_6 - \delta_n b_{13} + \delta_n \widehat{b}_4 \tag{A19}$$

The values of the b_i are calculated following Equations (A20), A21 and A22 and δ_n is equal to 1 to include the contribution of the out of the midline mass.

$$(b_1, b_2, b_3, b_4, b_5, b_6, b_7, b_8, b_9, b_{10}, b_{11}, b_{12}) = \int m_0 \left[1, y, x, y^2, x^2, xy, \overline{F}, y\overline{F}, x\overline{F}, \overline{F}^2, dx/ds, dy/ds\right] ds \tag{A20}$$

$$(b_{13}, b_{14}, b_{15}, b_{16}, b_{17}, b_{18}) = \int m_2 \left[(dx/ds)(dy/ds), (dx/ds)^2, (dy/ds)^2, r_t(dx/ds), r_t(dy/ds), r_t^2\right] ds \tag{A21}$$

$$(\widehat{b}_1, \widehat{b}_2\, \widehat{b}_3, \widehat{b}_4, \widehat{b}_5, \widehat{b}_6 \widehat{b}_7, \widehat{b}_8, \widehat{b}_9, \widehat{b}_{10}, \widehat{b}_{11}, \widehat{b}_{12}) = \int m_1 [r_t, dx/ds, dy/ds, ydy/ds - xdx/ds, \overline{F}dx/ds + yr_t, \overline{F}dy/ds - xr_t, \overline{F}r_t, ydx/ds, xdy/ds] ds \tag{A22}$$

The reduced mass terms are obtained from Equation (A23).

$$(m_0, m_1, m_2) = \sum_{k=1}^{N} \int_{h_{(k-1)}}^{h_{(k)}} \rho_{(k)} \left(1, n, n^2\right) dn \tag{A23}$$

Appendix B. Numerical solver 4th order Runge-Kutta method

In this appendix equations B1 and B2 of the four order Runge-Kutta method are provided.

$$\vec{f}_1 = \mathbf{M_A}\vec{x}_t + \vec{b} \qquad \vec{f}_2 = \mathbf{M_A}\left(\vec{x}_t + \frac{1}{2}\vec{f}_1 \Delta t_i\right) + \vec{b}$$
$$\vec{f}_3 = \mathbf{M_A}\left(\vec{x}_t + \frac{1}{2}\vec{f}_2 \Delta t_i\right) + \vec{b} \qquad \vec{f}_4 = \mathbf{M_A}\left(\vec{x}_t + \vec{f}_3 \Delta t_i\right) + \vec{b} \tag{B1}$$

$$\vec{x}_{t+1} = \vec{x}_t + \frac{1}{6}\left(\vec{f}_1 + 2\vec{f}_2 + 2\vec{f}_3 + \vec{f}_4\right)\Delta t_i \tag{B2}$$

References

Berdichevsky, V., Armanios, E., Badir, A., 1992. Theory of anisotropic thin-walled closed-cross-section beams. Compos. Eng. 2, 411–432.

Boudounit, H., Tarfaoui, M., Saifaoui, D., Nachtane, M., 2019. Structural analysis of offshore wind turbine blades using finite element method. Wind Eng. 44, 168–180.

Carrera, E., Filippi, M., Zappino, E., 2013. Free vibration analysis of rotating composite blades via Carrera Unified Formulation. Compos. Struct. 106, 317–325.

Carrión, M., Steijl, R., Woodgate, M., Barakos, G., Munduate, X., Gomez-Iradi, S., 2014. Aeroelastic analysis of wind turbines using a tightly coupled CFD-CSD method. J. Fluid Struct. 50, 392–415.

Chadra, R., Stemple, A.D., Chopra, I., 1990. Thin-walled composite beams under bending, torsional, and extensional loads. J. Aircraft 184, 872–882.

Chaviaropoulos, P., Hansen, M.O.L., 2000. Investigating three-dimensional and rotational effects on wind turbine blades by means of a Quasi3D Navier-Stokes solver. J. Fluid Eng. 122, 130–136.

Dowell, E., 2015. A Modern Course in Aeroelasticity. Springer.

Edenhofer, O., Pichs-Madruga, R., Sokona, Y., Seyboth, K., Kadner, S., Z, T., et al., 2011. Renewable Energy Sources and Climate Change Mitigation: Special Report of the Intergovernmental Panel on Climate Change, Technical Report. Cambridge University Press.

Farsadi, T., Asadi, D., Kurtaran, H., 2019. Flutter improvement of a thin walled wing engine system by applying curvilinear fiber path. Aero. Sci. Technol. 93, 105353.

Forcier, L.-C., Joncas, S., 2019. On the wind turbine blade loads from an aeroelastic simulation and their transfer to a three-dimensional finite element model of the blade. Wind Eng. 44, 577–595.

Gil, A., Tiseira, A., Quintero, P., Cremades, A., 2021. Prediction of the non-linear aeroelastic behavior of a cantilever flat plate and equivalent 2D model. Aero. Sci. Technol. 113, 106685.

Hand, M., Simms, D., Fingersh, L., Jager, D., Cotrell, J., Schreck, S., Larwood, S., 2001. Unsteady Aerodynamics Experiment Phase. National Renewable Energy Laboratory. VI: Wind Tunnel Test Configurations and Available Data Campaigns, Technical Report NREL/TP-500-29955.

Hansen, M., 2007. Aeroelastic instability problems for wind turbines. Wind Energy 10, 551–577.

Jacobson, M.Z., Masters, G.M., 2001. Exploiting wind versus coal. Science 293, 1438.

Jacobson, M.Z., Delucchi, M.A., Bazouin, G., Bauer, Z.A.F., Heavey, C.C., Fisher, E., Morris, S.B., Piekutowski, D.J.Y., Vencilla, T.A., Yeskooa, T.W., 2015. 100% clean and renewable wind, water, and sunlight (WWS) all-sector energy roadmaps for the 50 United States. Energy Environ. Sci. 8, 2093.

Kaviani, H.R., Nejat, A., 2021. Investigating the aeroelasticity effects on aeroacoustics and aerodynamics of a MW-class HAWT. J. Wind Eng. Ind. Aerod. 213, 104617.

Ledermann, C., Ermanni, P., Kelm, R., 2006. Dynamic CAD objects for structural optimization in preliminary aircraft design. Aero. Sci. Technol. 10, 601–610.

Lee, K., Huque, Z., Kommalapati, R., Han, S.-E., 2017. Fluid-structure interaction analysis of NREL phase VI wind turbine: aerodynamic force evaluation and structural analysis using FSI analysis. Renew. Energy 113, 512–531.

Li, S., Caracoglia, L., 2019. Surrogate Model Monte Carlo simulation for stochastic flutter analysis of wind turbine blades. J. Wind Eng. Ind. Aerod. 188, 43–60.

Li, Z., Wen, B., Dong, X., Peng, Z., Qu, Y., Zhang, W., 2020. Aerodynamic and aeroelastic characteristics of flexible wind turbine bladesunder periodic unsteady inflows. J. Wind Eng. Ind. Aerod. 197, 104057.

Librescu, L., Song, O., 2006. Thin-walled composite beams. In: Theory and Application. Springer.

Mahdi, E., Almabrouk, B., Hamouda, A., Mokhtar, A., Younus, R., Sultan, H., 2006. Utilization of composite's tensile properties for energy absorbing systems. Compos. Struct. 75, 29–38.

Manwell, J., McGowan, J., Rogers, A., 2009. Wind Energy Explained. Theory, Design and Application. Wiley.

Meng, M., Le, H., Rizvi, M., Grove, S., 2015. 3D FEA modelling of laminated composites in bending and their failure mechanisms. Compos. Struct. 119, 693–708.

Paquette, J., van Dam, J., Hughes, S., 2007. Structural Testing of 9m Carbon Fiber Wind Turbine Research Blades, 45th. AIAA Aerospace Sciences Meeting and Exhibit.

Plaza, B., Bardera, R., Visiedo, S., 2015. Comparison of BEM and CFD results for Mexico rotor aerodynamics. J. Wind Eng. Ind. Aerod. 145, 115–122.

Pourazarm, P., Caracoglia, L., Lackner, M., Modarres-Sadeghi, Y., 2016. Perturbation methods for the reliability analysis of wind-turbine blade failure due to flutter. J. Wind Eng. Ind. Aerod. 156, 159–171.

Qin, Z., Librescu, L., 2002. Static/Dynamic solutions and validation of a refined anisotropic thin-walled beam model. In: 43rd AIAA/ASME/ASCE/AHS/ASC Structures, Structural Dynamics and Materials Conference.

Rajpal, D., Gillebaart, E., Breuker, R.D., 2019. Preliminary aeroelastic design of composite wings subjected to critical gust loads. Compos. Struct. 85, 96–112.

Rogers, G., Kristof, J., 2003. Reducing operational and product costs through environmental accounting. Environ. Qual. Manag. 12, 17–42.

Sanches, L., Guimaraes, T.A., Marques, F.D., 2019. Aeroelastic tailoring of nonlinear typical section using the method of multiple scales to predict post-flutter stable LCOs. Aero. Sci. Technol. 90, 157–168.

Singh, S., Sivasubramanian, M., Reddy, A., Khatri, C., Nagarjuna, K., Kiran, A., 2012. Performance of NSM-FRP RC beams in flexure and shear using locally developed CFRP rebars. Int. J. Sustain. Mater. Struct. Syst. 1, 42–67.
Sorensen, N., Michelsen, J., Schreck, S., 2002. Navier-Stokes predictions of the NREL phase VI rotor in the NASA Ames 80 ft x 120 ft wind tunnel. Wind Energy 5, 151–169.
Stanford, B.K., Jutte, C.V., Wu, K.C., 2014. Aeroelastic benefits of tow steering for composite plates. Compos. Struct. 118, 416–422.
Theodorsen, T., 1935. General theory of aerodynamic instability and the mechanism of flutter. NACA 496.
Thomas, J.P., Dowell, E.H., Hall, K.C., 2002. Nonlinear inviscid aerodynamic effects on transonic divergence, flutter, and limit-cycle oscillations. AIAA J. 40, 638–646.
Torregrosa, A., Gil, A., Quintero, P., Ammirati, A., Denayer, H., Desmet, W., 2019a. Prediction of flow induced vibration of a flat plate located after a bluff wall mounted obstacle. J. Wind Eng. Ind. Aerod. 190, 23–39.
Torregrosa, A., Gil, A., Quintero, P., Tiseira, A., 2019b. Enhanced design methodology of a low power stall regulated wind turbine. BEMT and MRF-RANS combination and comparison with existing designs. J. Wind Eng. Ind. Aerod. 190, 230–244.
Touraj Farsadi, A.K., Sener, Özgün, 2017. Free vibration analysis of uniform and asymmetric composite pretwisted rotating thin walled beam, volume IMECE2017-70531, Proceedings of the International Mechanical Engineering Congress and Exposition. Adv. Aero. Technol. 3–9.
Venkatakrishnan, V., 1995. On the Convergence of Limiters and Convergence to Steady State Solutions. AIAA-93-0880.
Vijcic, I.T., Dimic, I.D., 2013. Microstructural characterization of glass-epoxy composites subjected to tensile testing. Acta Period. Technol. 44, 151–162.
Wang, L., Quant, R., Kolios, A., 2016. Fluid structure interaction modelling of horizontal-axis wind turbine blades based on CFD and FEA. J. Wind Eng. Ind. Aerod. 158, 11–25.
Weiss, J., Smith, W., 1995. Preconditioning applied to variable and constant density flows. AIAA J. 33, 2050–2057.
Weiss, J., Maruszewski, J., Smith, W., 1999. Implicit solution of preconditioned Navier-Stokes equations using algebraic multigrid. AIAA J. 37, 29–36.
Yao, S., Chetan, M., Griffith, D.T., Escalera Mendoza, A.S., Selig, M.S., Martin, D., Kianbakh, S., Johnson, K., Loth, E., 2021. Aero-structural design and optimization of 50 MW wind turbine with over 250-m blades. Wind Eng. 46, 273–295.